Earth and Planetary Science Letters 571 (2021) 117113

Contents lists available at ScienceDirect

Earth and Planetary Science Letters

www.elsevier.com/locate/epsl

Fast melt expulsion from crystal-rich mushes via induced anisotropic permeability

Boda Liu *, Cin-Ty Lee

Department of Earth, Environmental & Planetary Sciences, Rice University, United States of America

ARTICLE INFO

Article history:
Received 29 December 2020
Received in revised form 24 June 2021
Accepted 9 July 2021
Available online 2 August 2021
Editor: R. Hickey-Vargas

Keywords:
large silicic eruptions
melt extraction
consolidation
anisotropic permeability
melt texture
recharge

ABSTRACT

Catastrophic eruptions of rhyolitic super volcanoes require large volumes of silicic magma to be extracted from a crystal-rich mush at high rates. However, fast melt extraction is thought to be difficult because of the low permeability of mushes and the high viscosities of silicic melts. Here, we show that induced ephemeral high permeability pathways in the mush may be critical. During uniaxial compression of the mush, driven by the impingement of recharging magmas from below, melt within the mush can be redistributed preferentially into vertical melt pockets. This redistribution of melt can increase vertical permeability by a factor of 10-100 times, which leads to rapid expulsion of melt. As melt is expelled, the permeability rapidly declines. The end result is a fast, short-lived pulse of melt extraction that can grow a 1 km thick silicic magma reservoir in 10 kyr. Our analysis shows how the incursion of deep-seated magmas into the base of a crystal-rich mush in the crust can trigger the expulsion of silicic melts that may lead to an eruption.

1. Introduction

The extraction of melt from its crystal-rich source regions is a fundamental yet poorly understood process in the formation of large silicic reservoirs that feed eruptions (Hildreth, 1981; Bachmann et al., 2007). Substantial volumes of silicic melt can be stored in crystal-rich mushes in the crust (e.g. Hildreth, 1981; Hildreth and Fierstein, 2000; Bachmann and Bergantz, 2004; Schmandt et al., 2019). However, due to the high viscosity of the silicic melt (Lesher and Spera, 2015), many of the proposed mechanisms for melt extraction, such as compaction, settling or filter-pressing, are thought to be too slow (Lewis et al., 1949; Richardson and Zaki, 1954; Shaw, 1965; McKenzie, 1984; Holness, 2018), so that heat loss through the crust would freeze melts as they are extracted, preventing the assembly of a large silicic magma reservoir (Fialko and Simons, 2001; Annen, 2009; Gelman et al., 2013; Liu and Lee, 2020). There is, however, evidence that silicic volcanism is often associated with incursions of mafic magmas (Bachmann and Bergantz, 2006; Wark et al., 2007; Druitt et al., 2012). Because of their hotter temperatures, their deep origins, and their more primitive compositions, these mafic magmas are often invoked in rejuvenating silicic crystal mushes in the crust (Hildreth and Moorbath, 1988; Huang et al., 2015). Heating, re-melting, or the addition of volatiles, all driven by mafic recharge, could remobilize the crystal-rich mush, but exactly how interstitial melts are expelled from this mush is unclear. Here, we explore the possibility of whether the arrival of magmas at the base of crystal-rich mushes can change the permeability of the mush in a way that allows for rapid expulsion of interstitial melt. In particular, we explore how the development of anisotropic permeability can enhance melt extraction rates from crystal-rich mushes.

Existing permeability models consider hydrostatic conditions and thus implicitly assume isotropic melt distribution and permeability (von Bargen and Waff, 1986; Carman, 1997; Wark and Watson, 1998; Miller et al., 2014). However, melt preferred orientation (MPO) has been observed in deformed lab samples subjected to deviatoric stresses (Daines and Kohlstedt, 1997; Gleason et al., 1999). They showed that the long-axis of melt pockets are subparallel to the axis of maximum compression (σ_1) and that visible melt pockets commonly have long-axes oriented within 30° of σ_1 (Daines and Kohlstedt, 1997). In particular, melt pockets with long-axis parallel to σ_1 are also the thickest (Gleason et al., 1999; Sawyer, 2001). Similar MPO has been observed in natural samples where elongated melt pockets are preferentially oriented subperpendicular to the foliation (Rosenberg and Riller, 2000). These observations demonstrate that external forcing could impart anisotropic distribution of melt at the grain scale. Here, we develop an anisotropic permeability model and then investigate the dynamic feasibility of this mechanism in the application of extracting melt from the mush. We show that impingement of

* Corresponding author.
E-mail address: boda_liu@hotmail.com (B. Liu).

https://doi.org/10.1016/j.epsl.2021.117113
0012-821X/

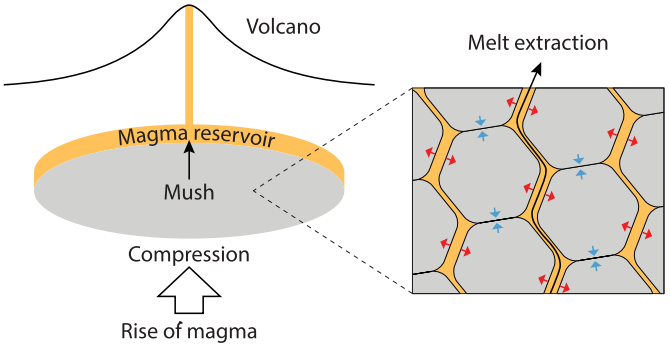

Fig. 1. Melt extraction of the crystal-rich source mush. As deeply derived magmas rise and impinge against the base of a crystal-rich mush. The mush is subjected to uniaxial compression, inducing a redistribution of melt that generates high vertical permeability pathways and rapid assembly of the magma reservoir. The melt inside the interstices of the crystal-rich mush needs to be extracted to accumulate an eruptible crystal-poor magma reservoir. Inside the crystal-rich source mush, a network of melt pockets bounded by grain boundaries forms the melt pathways. The thickness of high-angle melt pockets, which have long-axes subparallel to the axis of maximum compression, increases whereas the thickness of low-angle melt pockets decreases. Some low-angle melt pockets subparallel to the compression plane could close.

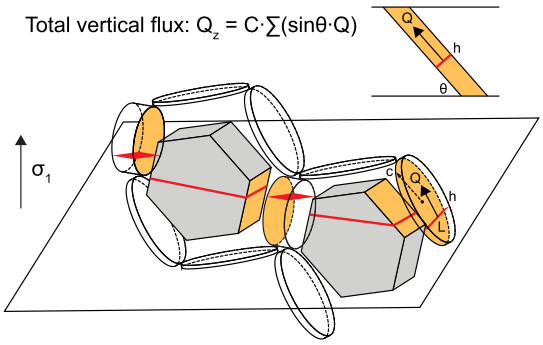

Fig. 2. A permeability model of connected melt disks. All grain boundaries are wetted and represented by melt disks of radius c and thickness h. The total vertical flux, Q_z, consists of the vertical component of melt fluxes through all melt disks (inserted expression, where the summation is over all possible orientations of melt pockets transected by a horizontal plane, C is the connectivity constant). The flux though a disk of thickness h (upper right inset) is calculated using the lubrication approximation. Under uniaxial compression (σ_1), vertical disks are thicker than flat disks.

deeply derived magmas at the base of shallow crystal mushes can provide the driving force for enhancing vertical permeability and thus significantly increase the rate of melt extraction (Fig. 1).

2. Permeability of a network of melt disks

We consider a crystal-rich magmatic mush where crystal fraction is high enough that the system is effectively locked and unable to freely convect. Locked magmatic mushes can have melt fractions up to 40% (Dufek and Bachmann, 2010), where all grain boundaries are wetted, forming an interconnected melt network (von Bargen and Waff, 1986; Mei et al., 2002; Rudge, 2018). To model the distribution of melt pockets, we approximate melt pockets as high aspect ratio (radius/thickness) cylindrical disks separating neighboring grains (Fig. 2). The diameter of a melt disk is controlled by the polygonal contact area between grains. The thickness of the melt disk is the width of the melt-filled gap between neighboring grains. Assuming the grain boundary has a tetragonal to hexagonal shape, the melt disk will be hinged to 4-6 triple junction edges and up to 8-12 other disks. According to percolation theory (Dienes, 1982), the melt network is considered highly connected if the melt pockets are connected to more than two neighbors. Therefore, the complex grain scale melt topology in the mush can be approximated by a network of melt-filled disks. Following the microscale permeability model of Dienes (1979), the flux through a plane inside the porous medium can be calculated as the weighted sum of melt fluxes through all melt disks transected by the plane (Fig. 2).

The flux of melt through a melt-filled disk strongly correlates with the thickness of the disk, h, and taking a lubrication approximation (Bird et al., 2002), is given by

$$Q = \gamma\left(\sin\theta\cdot\frac{h^2}{12\mu}\nabla P\right)A, \tag{1}$$

where Q is the volumetric flux through a melt disk; γ is a geometric factor for the curvature of the disk boundaries; θ is the orientation of the melt disk ($\theta = 0°$, horizontal; $\theta = 90°$, vertical); μ is the viscosity of the melt; ∇P is the pressure gradient (vertical as it is buoyancy driven); A is the cross-sectional area of the disk channel ($A = hL$); h is the thickness of the disk; and L is the length of the transect.

Motivated by the observation of relatively thick melt pockets at grain boundaries parallel to the axis of maximum compression (van der Molen and Paterson, 1979; Daines and Kohlstedt, 1997; Gleason et al., 1999; Rosenberg and Riller, 2000), we consider the case in which the thickness of melt disks is a function of the orientation, $h = h(\theta)$. The thickness function needs to satisfy the constraint of melt fraction or porosity (Dienes, 1979):

$$\phi = N_0\cdot\int_0^{\pi/2}\sin\theta d\theta\int_0^{\infty}p_c dc\cdot\pi c^2 h(\theta), \tag{2}$$

where ϕ is the porosity; N_0 is the number density of melt pockets; c is the radius of melt pockets. The volume of an individual melt disk is $\pi c^2 h(\theta)$, where the radius of the disk, c, is on the same length scale of the grain size. To account for a distribution of grain sizes, we assume that c has a log-normal distribution $p_c = \frac{1}{c_0}e^{-c/c_0}$ (Dienes, 1979) where c_0 is the average radius of melt disks. The average thickness of melt disks is proportional to the porosity, i.e. $\overline{h} = \frac{\phi}{2\pi N_0 c_0^2}$. The initial isotropic melt distribution corresponds to constant thickness of melt disks at all orientations, $h(\theta) = \overline{h}$.

A fundamental simplification here is that the mineral grains have equant shapes. Because the dominant mineral in silicic mushes are tabular-shaped plagioclases, the shape-preferred orientation of plagioclase would associate flattened melt pockets with large radius (Holness et al., 2017). However, as the mush is compressed vertically, those flattened melt pockets would effectively close and contribute little to the vertical permeability. For simplicity, we do not consider the effect of shape preferred orientation in the following discussion. The integration of textural data into the current model framework may help quantify the shape effect in future studies.

To keep track of the melt distribution during uniaxial compression, we parameterize the evolution of the texture in two stages. We assume that compression is faster than melt extraction so that the melt fraction is conserved in these two stages (we will come back to the kinetics later). In Stage I, the thickness of low angle-melt disks decreases while that of high-angle melt disks increases (Fig. 3). To describe the increase of the thickness with θ, it is helpful to formulate h as a linear function of θ in Stage I (Fig. 3). Once the thickness of the horizontal disk, $h(0)$, is specified, the slope of the line $h(\theta)$ can be constrained by the porosity. As $h(0)$ decreases in Stage I, the slope of the thickness function increases.

Once $h(0)$ is reduced to a critical value, the horizontal melt disk pinches off under surface tension, i.e. the two facing grain bound-

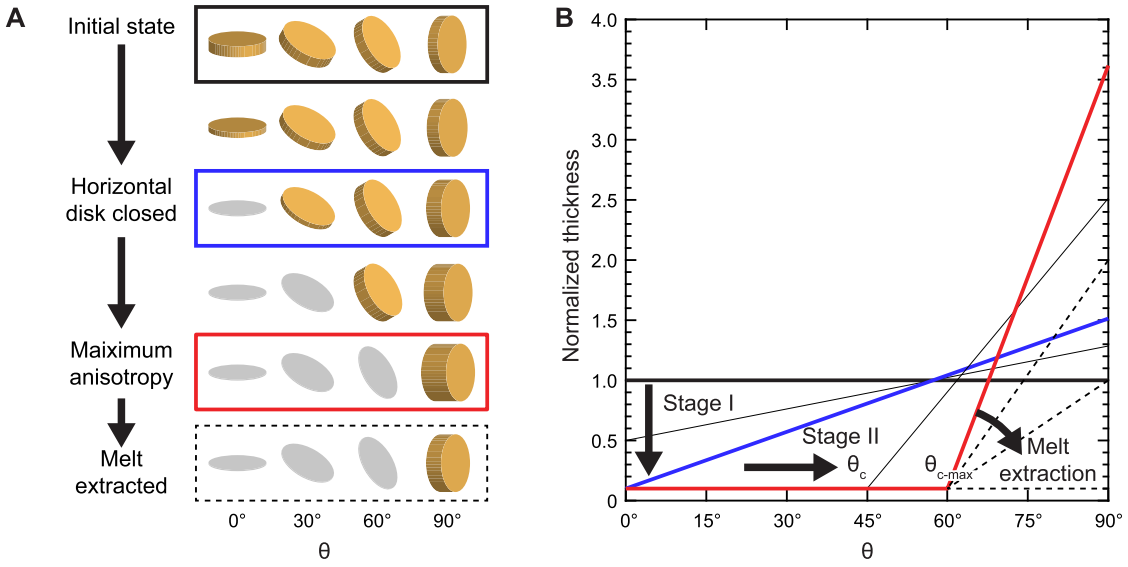

Fig. 3. The evolution of the melt distribution. The distribution of melt among melt disks of different orientations (**A**). Each row shows the thickness of four disks at θ =0°, 30°, 60°, and 90°. Initially, all disks have the same thickness. As the texture evolves to the next state, the thickness of these four representative disks changes, i.e. low-angle disks become thinner while high-angle disks dilate, preserving the total melt volume. When the thickness of the flat disk is thinned to a critical thickness (10% of the initial), the flat disk would be effectively closed for melt flow. After that, low-angle melt disks are gradually closing and high-angle disks are continuing dilating, still preserving total melt volume. Each state is represented by a closure angle θ_c. Disks with orientations less than θ_c are closed (marked gray). When θ_c increases to a maximum of $\theta_{c-\max}$ (60° as shown, see the text for details), the mush becomes too stiff to further close melt disks. At this point, melt extraction starts and causes the high-angle disks to begin contracting. The thickness of melt disk as a function of the orientation (**B**). The thickness is normalized by the initial thickness. The thick black line is the initial state. In Stage I, the thickness function is a line and the slope increases as the texture evolves. The thick blue line marks the end of Stage I. The system transitions to Stage II by closing low-angle disks with $\theta < \theta_c$, thus a flat line from $\theta = 0$ to θ_c. The most anisotropic texture (marked by thick red line) occurs when θ_c reaches the maximum, $\theta_{c-\max}$, beyond which melt in high-angle disks is extracted, causing the thickness function to rotate clockwise. (For interpretation of the colors in the figure(s), the reader is referred to the web version of this article.)

aries begin touching each other at the center, and the melt in the disk or the gap between the two grain boundaries will retreat to the edges and join neighboring disks (Waff and Bulau, 1979; von Bargen and Waff, 1986). Consequently, horizontal disks will become effectively closed for melt flow. As the compression of the mush continues, an increasing number of low-angle melt disks will thin below the critical thickness and progressively close. Therefore, Stage II of the melt redistribution is characterized by an increasing closure angle of low-angle melt disks, θ_c (Fig. 3). The critical thickness marks the transition of the distribution of melt from films at grain boundary to triple-junction tubes as the local melt fraction decreases below 3% (Hirth and Kohlstedt, 1995; Hammond and Humphreys, 2000; Mei et al., 2002). For a typical mush porosity of 40% (Hammond and Humphreys, 2000; Bachmann and Bergantz, 2004; Lee and Morton, 2015), the critical thickness would be ~10% of the initial thickness. In experiments of deformed basalt-olivine aggregates, most melt is concentrated into melt pockets with long-axis within 30° of σ_1 (Daines and Kohlstedt, 1997). Therefore, the closure angle could reach 60° and possibly higher.

Given the thickness function and the flux through individual melt disks (Eq. (1)), the bulk flux percolating the porous medium can be calculated by integrating the melt flux across all melt disks using the method of Dienes (1979). The sum of melt fluxes through all melt disks should be scaled down by an empirical constant ("connectivity", C) to represent the actual Darcy flux (Broadbent and Hammersley, 1957; Dienes, 1979, 1982). Then the vertical permeability can be derived from Darcy's law ($k_z = \frac{\mu}{\nabla P} \cdot Q_z$). Assuming the connectivity is a constant, C can be eliminated by normalizing the vertical permeability by the isotropic permeability,

$$k_z = \frac{16 k_{iso}}{3\pi} \int_0^{\pi/2} (\sin\theta)^4 \cdot \left(h(\theta)/\overline{h}\right)^3 d\theta, \tag{3}$$

where k_{iso} is a function of grain size (d) and porosity, $k_{iso} = \frac{d^2\phi^3}{180(1-\phi)^2}$ (Carman, 1997). The geometric factor in Eq. (1) is canceled in the normalization.

The evolution of vertical permeability can be tracked by substituting the instantaneous thickness function into the permeability model (Eq. (3)). Results (Fig. 4a) show that the permeability can be increased by up to two times in Stage I until the thickness of the horizontal melt disks decrease to the critical thickness. As compression continues, the textural evolution proceeds to Stage II by gradually closing low angle melt disks. The maximum vertical permeability would depend on the maximum closure angle, $\theta_{c-\max}$. Using an experimentally inferred lower bound for $\theta_{c-\max}$ of 60° (Daines and Kohlstedt, 1997), the vertical permeability could increase to ten times that of the isotropic permeability (Fig. 4a). The exact meaning of $\theta_{c-\max}$ is not clear for the moment as the dynamic process associated with melt redistribution has not been evaluated (see next section). Nevertheless, the abovementioned process of redistributing melt from low-angle melt disks to high-angle ones could have significant effects on permeability along the direction of maximum compression.

3. The dynamic cost of melt redistribution

The redistribution of melts requires work to change the thickness of melt disks. Therefore, we need to consider the rate of energy dissipation required for the texture to evolve. We calculate the rate of energy dissipation by summing up the work on all melt disks. The rate of energy dissipation per volume can be determined by calculating the amount of work done on dilating or contracting the disks per unit time

$$\frac{dW}{dt} = N_0 \int_0^{\pi/2} \sin\theta d\theta \int_0^{\infty} p_c dc \cdot F \frac{dh}{dt}. \tag{4}$$

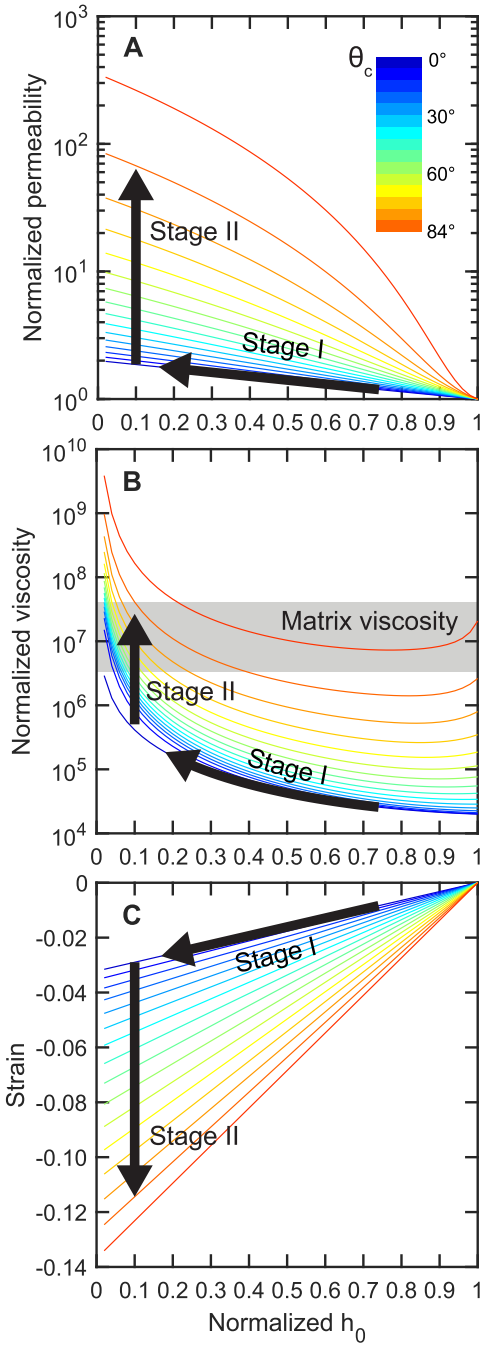

Fig. 4. Permeability, effective viscosity, and strain. The evolution of vertical permeability is normalized by the isotropic permeability (**A**). Effective viscosity is normalized by the melt viscosity, 10^5 Pa·s (Lesher and Spera, 2015) (**B**). The vertical strain of the mush under uniaxial compression (**C**). The porosity is assumed constant in Stages I and II. The absolute value of porosity would not affect these normalized values. The color represents the closure angle from 0° to 84°. Thick black arrows mark the two-stage evolution that transitions at $h_0 = 0.1\bar{h}$. The redistribution of melt would stop when the effective viscosity associated with melt redistribution reaches the viscosity for plastic deformation of the solid matrix (van der Molen and Paterson, 1979; Mei et al., 2002). The closure angle at the end of Stage II is between 60° to 80°. Results are included in the Supplementary Table S1.

For a single melt film, the normal force required to change the thickness can be approximated by lubrication theory $F = \frac{3\mu c^4}{2h^3}\frac{dh}{dt}$ (Bird et al., 2002). The lubrication approximation is especially accurate for thin melt disks, which are the ones that consume the most energy and are thus most difficult to compress/dilate. Therefore, using a lubrication approximation in Eq. (4) provides a reasonable estimate of viscous dissipation.

The vertical strain rate can be calculated by integrating the rate of volume inflation/deflation of all melt pockets:

$$\frac{d\varepsilon}{dt} = N_0 \int_0^{\pi/2} \sin\theta d\theta \int_0^{\infty} p_c dc \cdot \pi c^2 \frac{dh}{dt} \cdot \cos\theta. \quad (5)$$

Then the effective viscosity of the bulk mush, defined as $\eta = \left(\frac{dW}{dt}\right) / \left(\frac{d\varepsilon}{dt}\right)^2$, can be calculated by substituting the thickness functions into Eqs. (4)–(5). In Stage I, the effective viscosity increases from 2×10^4 times the melt viscosity to 4×10^5 times the melt viscosity (Fig. 4b). In Stage II, the effective viscosity increases dramatically, reaching 6×10^6 times the melt viscosity at $\theta_c = 60°$ when the vertical shortening reaches 10%. Assuming a melt viscosity of 5×10^5 Pa·s, the effective viscosity of the mush increases from 10^{10} Pa·s at the onset of compression to 10^{12} Pa·s at 10% vertical shortening.

The predicted low effective viscosity at the beginning is purely due to viscous dissipation of the melt and thus should be regarded as a lower bound. There is the possibility that redistribution of melt can be hindered by plastic flow of the solid matrix in the form of grain boundary sliding or lattice deformation (Kohlstedt et al., 2000; Rosenberg, 2001; Antony, 2007; Wieser et al., 2020). However, since all grain boundaries would be wetted at typical mush porosities of greater than 30% (Hirth and Kohlstedt, 1995; Mei et al., 2002; Bachmann and Bergantz, 2004), contacts between mineral grains would be lubricated and the relative tangential motion of minerals would be minimally hindered. Indeed, there is minimal microstructural evidence of plastic deformation in plagioclase-dominated cumulates (Holness et al., 2017). Therefore, deformation before consolidation would be accommodated by redistribution of melt, and energy dissipation would be dominated by viscous dissipation in the interstitial melts. The prediction of small effective viscosity for the consolidating mush would be a strict lower bound. The redistribution of melt would become increasingly difficult and terminate when the effective viscosity of the mush reaches the viscosity for plastic deformation of the solid matrix, $\sim 10^{12}$ Pa·s (van der Molen and Paterson, 1979; Mei et al., 2002). The maximum closure angle $\theta_{c-\max}$ would be 60° to 80° (Fig. 4b). The mush would be consolidated after reaching $\theta_{c-\max}$. Further deformation of the mush would be rate-limited by plastic deformation of the solid matrix.

We now consider the case in which the mush is subjected to compression from below associated with the impingement of deeply derived magma at the base of the mush. Such a scenario is commonly envisioned for long-lived magmatic systems as these systems lie above active mafic magma production in the mantle, such as in subduction zones or above upwelling mantle. The upward migration of mantle-derived magma to the lower crustal mush would induce a stress on the crust within which the crystal-rich source mush resides. We follow the method of Jellinek and DePaolo (2003) to estimate the induced stress of an inflating lower crustal mush on the overlying crust, $\Delta P = \frac{4\mu_s Q_m}{\pi l^3} \simeq 4 \times 10^3$ Pa, where the viscosity of crustal wall rock μ_s is 10^{15} Pa·s (van der Molen and Paterson, 1979), the volume injection rate Q_m is 0.1 km^3/yr (Spera and Crisp, 1981), and the length scale of the magma body l is 10 km (the thickness of lower crust). Under such deviatoric stress, the mush with an effective viscosity of $\eta = 10^{10} - 10^{12}$ Pa·s would be shortened by 10% and consolidate within one year ($t_{consolidate} = 0.1\eta/\Delta P$). Therefore, the deformation and consolidation of the mush could be a natural consequence of deeply derived magma pushing from below on the source mush. This mechanical and textural response is rapid and is able to produce high vertical permeability.

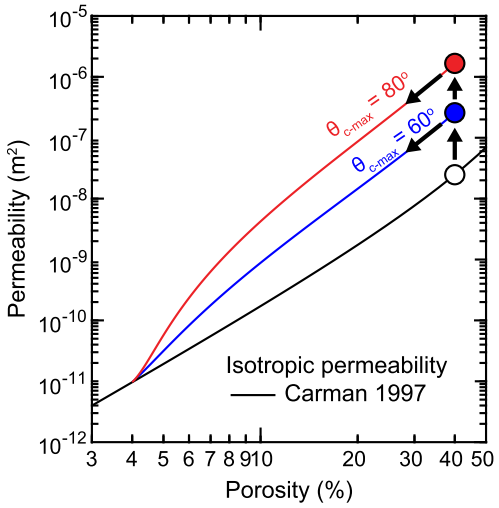

Fig. 5. The current anisotropic permeability model vs. the isotropic permeability model (Carman, 1997). The average grain size is 5 mm (Bachmann and Bergantz, 2004). The open circle marks the initial state with 40% porosity. Under axial compression, the mush deforms quickly and the vertical permeability increases until the mush becomes too stiff to further redistribute melt (filled circles, $\theta_{c-\max} = 60°$ to 80°). Melt extraction then reduces the porosity and thus the permeability (red and blue trends). The anisotropic permeability drops faster than the isotropic model because high-angle melt disks in the mush are preferentially thinned. The permeability will converge to the isotropic model when all melt disks are thinned to the critical thickness, $0.1\bar{h}$, which corresponds to 10% of the original melt fraction.

4. Melt extraction with anisotropic permeability

Once the mush consolidates and the highly anisotropic texture forms, melts in high-angle melt disks would be preferentially extracted. We will later see that the time scale of consolidation ($t_{consolidate} \sim 1$ yr) is much shorter than the time scale of melt extraction (>10 kyr). Therefore, melt extraction during consolidation can be neglected and we model the melt extraction starting from the consolidation. The evolution of the melt distribution during melt extraction can be specified by rotating the high-angle segment of the thickness function clockwise about the kink at $\theta_{c-\max}$ (Fig. 3). The vertical permeability is calculated by substituting the instantaneous thickness function into Eq. (3). The melt extraction rate would slow down as melt is extracted and the vertical permeability decreases (Fig. 5). The compaction length is small (~1 m) and thus the depth profile of the porosity in the mush would be almost uniform at any given time (McKenzie, 1984).

Considering a thick ($H = 10$ km or 20 km) mush layer, the rate of porosity reduction is proportional to the Darcy flux, $\frac{d\phi}{dt} = -J/H$, where the Darcy flux is buoyancy-driven, $J = \frac{k_z}{\mu}\Delta\rho g$. We compare the current anisotropic permeability model with the isotropic permeability model (Carman, 1997), keeping relevant parameters the same (melt viscosity 5×10^5 Pa·s, density contrast 340 kg/m^3, Lesher and Spera, 2015). The choices of initial porosity ($\phi_0 = 0.4$) and the average grain size (5 mm) are upper bound estimates (Bachmann and Bergantz, 2004; Lee and Morton, 2015). The growth rate of the magma reservoir is the Darcy flux J and the thickness of the magma reservoir is $H_{MR} = H(\phi_0 - \phi)$.

Results show that a 1 km-thick magma reservoir can assemble in 10 kyr from an underlying mush if the permeability in the mush is highly anisotropic (Fig. 6). For comparison, if melt extraction operates with isotropic permeability (Carman, 1997), the porosity barely changes, the melt extraction rate is persistently slow (~10^{-10} m/s), and the accumulated magma reservoir is thin (200 m) in the 50 kyr simulation. Thermal models predict that the magma injection rate has to be at least ~10^{-9} m/s otherwise the melt layer will freeze instantaneously (Annen et al., 2008; Annen, 2009; Gelman et al., 2013). If there is an active hydrothermal system in the shallow crust, even higher growth rates are needed to prevent freezing (Liu and Lee, 2020). Cases with isotropic permeability are unable to exceed these minimum growth rates, but the initial melt extraction rate with current anisotropic permeability can. After the porosity of the mush decreases and the melt extraction rate decays, the growth of the magma reservoir slows down and the magma undergoes cooling and crystallization.

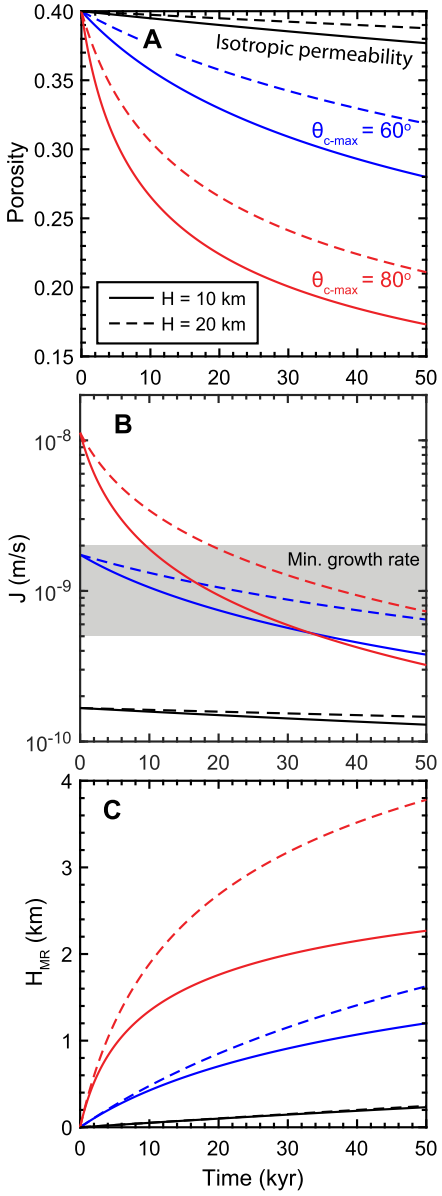

Fig. 6. Modeling melt extraction with anisotropic permeability. The evolution of the mush porosity (**A**), the melt extraction rate (**B**), and the thickness of the resultant, overlying melt reservoir (**C**). Results calculated using the isotropic permeability (Carman, 1997) are in black. Results calculated using the current permeability model are in blue and red. The average grain size is 5 mm for all simulations. The range of minimum growth rate is derived from thermal models (Annen et al., 2008; Annen, 2009; Gelman et al., 2013).

5. Conclusions and outlook

In summary, when a crystal-rich mush is compressed from below, such as by the impingement of recharging magmas, vertical permeability can be enhanced by 100-1000 times as interstitial melts are redistributed from horizontal to vertical melt pockets. This permeability anisotropy allows for melts to be rapidly ex-

pelled from the mush, but as melt is expelled, vertical permeability decreases. The end-result is a rapid but brief pulse of melt expulsion. Importantly, within 10 kyr, the pulse of melt expulsion can assemble a 1 km-thick, 500 km^3 silicic reservoir, which could set the conditions for a super eruption (Druitt et al., 2012; Gregg et al., 2012). We speculate that the eruption of super volcanoes could be controlled by ephemeral changes in the stress state within the upper and middle crust where crystal-rich mushes reside, presumably as a result of major recharge events. Fast melt extraction through highly permeable, yet short-lived vertical pathways could reconcile the coexistence of long-lived source mushes and the occasional rapid assembly of crystal-poor magma reservoirs (Cooper and Kent, 2014; Barboni et al., 2016; Ackerson et al., 2018; Jackson et al., 2018).

Although we have focused on vertical compression, horizontal extension (such as at mid-ocean ridges or continental rifts) would have similar effects on vertical permeability. In fact, most silicic calderas occur in regions of local extension (Hughes and Mahood, 2008). In compressional or neutral tectonic environment, vertical compression of the mush can also occur locally by occasional incursion of deeply derived magma into upper crust. The perturbation of the stress state in the upper crust could temporally dominate the large-scale tectonic environment. Current analysis suggests that a slight differential stress (4×10^3 Pa) and a small accumulated strain (10%) are able to significantly increase the vertical permeability. Therefore, induced anisotropic permeability may be a widespread process in a multitude of geological environments. Future studies on the trans-crustal magmatic system, including the prediction of super volcanoes, should not ignore the role of deep-seated external forcing, which changes the permeability structure of magmatic mushes and thus allows for rapid, but episodic extraction of melts.

CRediT authorship contribution statement

Boda Liu: Developed the model, produced the results, interpreted the results, and wrote the manuscript. **Cin-Ty Lee:** Interpreted the results and wrote the manuscript.

Declaration of competing interest

The authors declare that they have no known competing financial interests or personal relationships that could have appeared to influence the work reported in this paper.

Acknowledgements

We thank H. Gonnermann, P. Phelps, J. Jordan, and Y. Liang for the discussions. The manuscript benefited from constructive reviews by F. Wadsworth. B. L. was supported by Wiess Postdoctoral Fellowship at Rice University. C.-T. L. was supported by NSF grant EAR-1753599.

Appendix A. Supplementary material

The code to calculate the permeability, viscosity, and the strain of the mush is provided in the supplementary material. The resulted data are included in Supplementary Table S1. Supplementary material related to this article can be found online at https://doi.org/10.1016/j.epsl.2021.117113.

References

Ackerson, M.R., Mysen, B.O., Tailby, N.D., Watson, E.B., 2018. Low-temperature crystallization of granites and the implications for crustal magmatism. Nature 559, 94–97.

Annen, C., 2009. From plutons to magma chambers: thermal constraints on the accumulation of eruptible silicic magma in the upper crust. Earth Planet. Sci. Lett. 284, 409–416.

Annen, C., Pichavant, M., Bachmann, O., Burgisser, A., 2008. Conditions for the growth of a long-lived shallow crustal magma chamber below Mount Pelee volcano (Martinique, Lesser Antilles Arc). J. Geophys. Res., Solid Earth 113.

Antony, S.J., 2007. Link between single-particle properties and macroscopic properties in particulate assemblies: role of structures within structures. Philos. Trans. R. Soc. A, Math. Phys. Eng. Sci. 365 (1861), 2879–2891.

Bachmann, O., Bergantz, G.W., 2004. On the origin of crystal-poor rhyolites: extracted from batholithic crystal mushes. J. Petrol. 45, 1565–1582.

Bachmann, O., Bergantz, G.W., 2006. Gas percolation in upper-crustal silicic crystal mushes as a mechanism for upward heat advection and rejuvenation of near-solidus magma bodies. J. Volcanol. Geotherm. Res. 149, 85–102.

Bachmann, O., Miller, C.F., de Silva, S.L., 2007. The volcanic–plutonic connection as a stage for understanding crustal magmatism. J. Volcanol. Geotherm. Res. 167, 1–23.

Barboni, M., Boehnke, P., Schmitt, A.K., Harrison, T.M., Shane, P., Bouvier, A.-S., Baumgartner, L., 2016. Warm storage for arc magmas. Proc. Natl. Acad. Sci. 113, 13959–13964.

Bird, R., Stewart, W., Lightfoot, E., 2002. Transport Phenomena, second edition. John Wiley & Sons, Inc.

Broadbent, S.R., Hammersley, J.M., 1957. Percolation processes: I. Crystals and mazes. Math. Proc. Camb. Philos. Soc. 53, 629–641.

Carman, P.C., 1997. Fluid flow through granular beds. Chem. Eng. Res. Des. 75, S32–S48.

Cooper, K.M., Kent, A.J.R., 2014. Rapid remobilization of magmatic crystals kept in cold storage. Nature 506, 480.

Daines, M.J., Kohlstedt, D.L., 1997. Influence of deformation on melt topology in peridotites. J. Geophys. Res., Solid Earth 102, 10257–10271.

Dienes, J.K., 1979. On the inference of crack statistics from observations on an outcropping. In: 20th U.S. Symposium on Rock Mechanics (USRMS). American Rock Mechanics Association, Austin, Texas, p. 6.

Dienes, J.K., 1982. Permeability, percolation and statistical crack mechanics. In: The 23rd U.S Symposium on Rock Mechanics (USRMS). American Rock Mechanics Association, Berkeley, California, p. 9.

Druitt, T.H., Costa, F., Deloule, E., Dungan, M., Scaillet, B., 2012. Decadal to monthly timescales of magma transfer and reservoir growth at a caldera volcano. Nature 482, 77.

Dufek, J., Bachmann, O., 2010. Quantum magmatism: magmatic compositional gaps generated by melt-crystal dynamics. Geology 38, 687–690.

Fialko, Y., Simons, M., 2001. Evidence for on-going inflation of the Socorro Magma Body, New Mexico, from interferometric synthetic aperture radar imaging. Geophys. Res. Lett. 28, 3549–3552.

Gelman, S.E., Gutiérrez, F.J., Bachmann, O., 2013. On the longevity of large upper crustal silicic magma reservoirs. Geology 41, 759–762.

Gleason, G.C., Bruce, V., Green, H.W., 1999. Experimental investigation of melt topology in partially molten quartzo-feldspathic aggregates under hydrostatic and non-hydrostatic stress. J. Metamorph. Geol. 17, 705–722.

Gregg, P.M., de Silva, S.L., Grosfils, E.B., Parmigiani, J.P., 2012. Catastrophic caldera-forming eruptions: thermomechanics and implications for eruption triggering and maximum caldera dimensions on Earth. J. Volcanol. Geotherm. Res. 241–242, 1–12.

Hammond, W.C., Humphreys, E.D., 2000. Upper mantle seismic wave velocity: effects of realistic partial melt geometries. J. Geophys. Res., Solid Earth 105, 10975–10986.

Hildreth, W., 1981. Gradients in silicic magma chambers: implications for lithospheric magmatism. J. Geophys. Res., Solid Earth 86, 10153–10192.

Hildreth, W., Fierstein, J., 2000. Katmai volcanic cluster and the great eruption of 1912. Geol. Soc. Am. Bull. 112, 1594–1620.

Hildreth, W., Moorbath, S., 1988. Crustal contributions to arc magmatism in the Andes of Central Chile. Contrib. Mineral. Petrol. 98, 455–489.

Hirth, G., Kohlstedt, D.L., 1995. Experimental constraints on the dynamics of the partially molten upper mantle: deformation in the diffusion creep regime. J. Geophys. Res., Solid Earth (1978–2012) 100, 1981–2001.

Holness, M.B., 2018. Melt segregation from silicic crystal mushes: a critical appraisal of possible mechanisms and their microstructural record. Contrib. Mineral. Petrol. 173, 48.

Holness, M.B., Vukmanovic, Z., Mariani, E., 2017. Assessing the role of compaction in the formation of adcumulates: a microstructural perspective. J. Petrol. 58, 643–673.

Huang, H.-H., Lin, F.-C., Schmandt, B., Farrell, J., Smith, R.B., Tsai, V.C., 2015. The Yellowstone magmatic system from the mantle plume to the upper crust. Science 348, 773–776.

Hughes, G.R., Mahood, G.A., 2008. Tectonic controls on the nature of large silicic calderas in volcanic arcs. Geology 36, 627–630.

Jackson, M.D., Blundy, J., Sparks, R.S.J., 2018. Chemical differentiation, cold storage and remobilization of magma in the Earth's crust. Nature 564, 405–409.

Jellinek, A.M., DePaolo, D.J., 2003. A model for the origin of large silicic magma chambers: precursors of caldera-forming eruptions. Bull. Volcanol. 65, 363–381.

Kohlstedt, D.L., Bai, Q., Wang, Z.-C., Mei, S., 2000. Rheology of partially molten rocks. In: Physics and Chemistry of Partially Molten Rocks. Springer, pp. 3–28.
Lee, C.-T.A., Morton, D.M., 2015. High silica granites: terminal porosity and crystal settling in shallow magma chambers. Earth Planet. Sci. Lett. 409, 23–31.
Lesher, C.E., Spera, F.J., 2015. Thermodynamic and transport properties of silicate melts and magma. In: Sigurdsson, H. (Ed.), The Encyclopedia of Volcanoes, second edition. Academic Press, Amsterdam, pp. 113–141. Chapter 5.
Lewis, W.K., Gilliland, E.R., Bauer, W.C., 1949. Characteristics of fluidized particles. Ind. Eng. Chem. 41, 1104–1117.
Liu, B., Lee, C.-T., 2020. Large silicic eruptions, episodic recharge, and the transcrustal magmatic system. Geochem. Geophys. Geosyst. 21, e2020GC009220.
McKenzie, D., 1984. The generation and compaction of partially molten rock. J. Petrol. 25, 713–765.
Mei, S., Bai, W., Hiraga, T., Kohlstedt, D.L., 2002. Influence of melt on the creep behavior of olivine–basalt aggregates under hydrous conditions. Earth Planet. Sci. Lett. 201, 491–507.
Miller, K.J., Zhu, W.-l., Montési, L.G.J., Gaetani, G.A., 2014. Experimental quantification of permeability of partially molten mantle rock. Earth Planet. Sci. Lett. 388, 273–282.
Richardson, J., Zaki, W., 1954. Sedimentation and fluidisation. Part 1. Trans. Inst. Chem. Eng. 32, 35–53.
Rosenberg, C.L., 2001. Deformation of partially molten granite: a review and comparison of experimental and natural case studies. Int. J. Earth Sci. 90, 60–76.
Rosenberg, C.L., Riller, U., 2000. Partial-melt topology in statically and dynamically recrystallized granite. Geology 28, 7–10.
Rudge, J.F., 2018. Textural equilibrium melt geometries around tetrakaidecahedral grains. Proc. R. Soc., Ser. A, Math. Phys. Eng. Sci. 474, 20170639.
Sawyer, E.W., 2001. Melt segregation in the continental crust: distribution and movement of melt in anatectic rocks. J. Metamorph. Geol. 19, 291–309.
Schmandt, B., Jiang, C., Farrell, J., 2019. Seismic perspectives from the western U.S. on magma reservoirs underlying large silicic calderas. J. Volcanol. Geotherm. Res. 384, 158–178.
Shaw, H.R., 1965. Comments on viscosity, crystal settling, and convection in granitic magmas. Am. J. Sci. 263, 120–152.
Spera, F.J., Crisp, J.A., 1981. Eruption volume, periodicity, and caldera area: relationships and inferences on development of compositional zonation in silicic magma chambers. J. Volcanol. Geotherm. Res. 11, 169–187.
van der Molen, I., Paterson, M.S., 1979. Experimental deformation of partially-melted granite. Contrib. Mineral. Petrol. 70, 299–318.
von Bargen, N., Waff, H.S., 1986. Permeabilities, interfacial areas and curvatures of partially molten systems: results of numerical computations of equilibrium microstructures. J. Geophys. Res., Solid Earth 91, 9261–9276.
Waff, H.S., Bulau, J.R., 1979. Equilibrium fluid distribution in an ultramafic partial melt under hydrostatic stress conditions. J. Geophys. Res., Solid Earth 84.
Wark, D., Hildreth, W., Spear, F., Cherniak, D., Watson, E., 2007. Pre-eruption recharge of the Bishop magma system. Geology 35, 235–238.
Wark, D.A., Watson, E.B., 1998. Grain-scale permeabilities of texturally equilibrated, monomineralic rocks. Earth Planet. Sci. Lett. 164, 591–605.
Wieser, P.E., Edmonds, M., Maclennan, J., Wheeler, J., 2020. Microstructural constraints on magmatic mushes under Kīlauea Volcano, Hawai'i. Nat. Commun. 11 (1), 14.